JOURNAL OF APPLIED CRYSTALLOGRAPHY

ISSN 1600-5767

# Nanoscale order in the frustrated mixed conductor $La_{5.6}WO_{12-\delta}$

Tobias Scherb,[a]* Simon A. J. Kimber,[b] Christiane Stephan,[c,d] Paul F. Henry,[e] Gerhard Schumacher,[a] Sonia Escolástico,[f] José M. Serra,[f] Janka Seeger,[g] Justus Just,[a] Adrian H. Hill[b]‡ and John Banhart[a,h]

[a]Helmholtz-Zentrum Berlin für Materialien und Energie (HZB), Hahn-Meitner-Platz 1, 14109 Berlin, Germany, [b]European Synchrotron Radiation Facility (ESRF), 6 rue Jules Horowitz, BP 220, 38043 Grenoble Cedex 9, France, [c]Freie Universität Berlin, Malteserstrasse 74-100, 12249 Berlin, Germany, [d]Bundesanstalt für Materialforschung und -prüfung (BAM), Unter den Eichen 87, 12205 Berlin, Germany, [e]European Spallation Source ESS AB, Box 176, 22100 Lund, Sweden, [f]Instituto de Tecnología Química (UPV-CSIC), Avenida los Naranjos s/n, 46022 Valencia, Spain, [g]Forschungszentrum Jülich GmbH (FZJ), 52425 Jülich, Germany, and [h]Technische Universität Berlin, Hardenbergstrasse 36, 10623 Berlin, Germany. *Correspondence e-mail: tobias.scherb@helmholtz-berlin.de

Received 2 February 2016
Accepted 15 April 2016

Edited by K. Chapman, Argonne National Laboratory, USA

‡ Current address: Johnson Matthey Technology Centre, Intercat-JM Technology Centre, 107 Eli Whitney Boulevard, Savannah, GA 31408, USA.

**Keywords:** neutron diffraction; X-ray diffraction; pair distribution function; EXAFS; proton conductors; $La_{5.6}WO_{12-\delta}$.

**Supporting information**: this article has supporting information at journals.iucr.org/j

This article reports a comprehensive investigation of the average and local structure of $La_{5.6}WO_{12-\delta}$, which has excellent mixed proton, electron and oxide ion conduction suitable for device applications. Synchrotron X-ray and neutron powder diffraction show that a cubic fluorite supercell describes the average structure, with highly disordered lanthanum and oxide positions. On average, the tungsten sites are sixfold coordinated and a trace [3.7 (1.3)%] of anti-site disorder is detected. In addition to sharp Bragg reflections, strong diffuse neutron scattering is observed, which hints at short-range order. Plausible local configurations are considered and it is shown that the defect chemistry implies a simple 'chemical exchange' interaction that favours ordered $WO_6$ octahedra. The local model is confirmed by synchrotron X-ray pair distribution function analysis and EXAFS experiments performed at the La $K$ and W $L_3$ edges. It is shown that ordered domains of ~3.5 nm are found, implying that mixed conduction in $La_{5.6}WO_{12-\delta}$ is associated with a defective glassy-like anion sublattice. The origins of this ground state are proposed to lie in the non-bipartite nature of the face-centred cubic lattice and the pairwise interactions which link the orientation of neighbouring octahedral $WO_6$ sites. This 'function through frustration' could provide a means of designing new mixed conductors.

## 1. Introduction

Ionic conductors, which transport charge by the motion of ionic species, are essential components in next-generation energy sources such as fuel cells and for separating hydrogen from mixed gas streams in fossil fuel power plants (Yang *et al.*, 2009; Fabbri *et al.*, 2010; Norby, 2007; Jordal *et al.*, 2004). Such applications have demanding requirements for ionic conductors that can withstand high temperatures and reactive atmospheres. Proton-conducting ceramic membranes will also play a vital role in challenging industrial processes such as gas-to-liquid conversion, selective dehydrogenation, water–gas shift reaction and ammonia synthesis thanks to their integration in catalytic membrane reactors (Jordal *et al.*, 2004; Fontaine *et al.*, 2007; Li *et al.*, 2002). The crystal structure of mixed conductors plays a crucial role. A combination of a crystalline sublattice, to provide rigidity, and a defective, short-range correlated sublattice of charge carriers would be ideal (Kreuer, 2003). Oxygen vacancies in particular are needed for proton conduction and are usually created by doping. However, this synthetic strategy entails a delicate

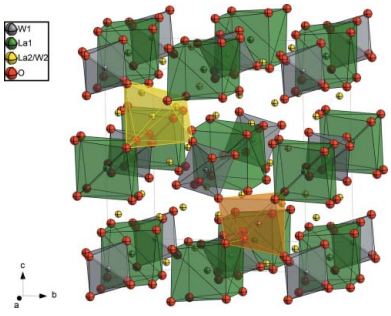

balancing act (Fabbri *et al.*, 2010; Aricò *et al.*, 2005; Pergolesi *et al.*, 2010; Malavasi *et al.*, 2010) since the creation of defects by doping causes structural inhomogeneities, such as cation size and charge mismatches or grain boundaries, which may trap charge carriers (Hempelmann *et al.*, 1998). High-quality grain-boundary-free thin films are thus needed for optimum performance (Pergolesi *et al.*, 2010). Proton conduction is also favoured by high-symmetry lattices. However, in the commonly studied $ABO_3$ perovskite materials, the tolerance factor required for cubic structures presupposes large *A*-site cations such as barium, which result in chemical instabilities in the acidic atmospheres found in typical applications. This is especially true for high-temperature applications, such as the removal of hydrogen from syngas mixtures, which are needed to support the transition to a hydrogen-based economy and to improve the efficiency of current sustainable energy production (Norby, 2007).

Rare earth tungstates with the general formula $Ln_6WO_{12}$ (Ln = rare earth) are promising materials as they show several ordered crystal structures as a function of rare earth size, and an excellent combination of proton and electron conductivity (McCarthy *et al.*, 1972; Shimura *et al.*, 2001; Escolástico *et al.*, 2009; Haugsrud, 2007). The ceramic $La_{6-x}WO_{12-\delta}$ ($0.3 < x < 0.7$) provides the highest proton conductivity and fulfils the requirements for an efficient mixed ionic electronic conductor. The physical properties shown by $La_{6-x}WO_{12-\delta}$ membranes are ideal for applications (Solís *et al.*, 2011; Escolástico *et al.*, 2013; Seeger *et al.*, 2013; Magrasó & Haugsrud, 2014). Despite many attempts, the polymorphism and extremely subtle structural distortions shown by this family of materials have prevented accurate solution of the crystal structure. Various reports of disordered pyrochlore or ordered defect fluorite-like structures have previously been published (McCarthy *et al.*, 1972; Chang & Phillips, 1964). Most recently, Magrasó *et al.* (2009, 2012, 2013) have published three different structures for $La_{5.6}WO_{12-\delta}$ using neutron and X-ray powder diffraction. These authors ultimately proposed a cubic fluorite-type structure with a $2a \times 2a \times 2a$ superlattice caused by cation ordering, and noted that single-phase specimens were only observed for La/W ratios between 5.3 and 5.7 (Magrasó *et al.*, 2009). Density functional theory (DFT) calculations and recent high-temperature neutron diffraction experiments have updated the former model (Magrasó *et al.*, 2012, 2013; Kalland *et al.*, 2013). However, the exact relationship between the average and local crystal structure, microstructure, and proton conductivity remains unresolved. Most fundamentally, it is also presently unclear why the cubic phases of $Ln_{6-x}WO_{12-\delta}$ stoichiometry are so disordered, given the presence of completely ordered phases very close by in the phase diagram. For example, orthorhombic phases of stoichiometry $Ln_{10}W_2O_{21}$ and rhombohedral $Ln_6WO_{12}$ phases form for smaller rare earths. Both of these structure types have ordered arrangements of anion defects and hence are very poor ionic conductors (Scherb, 2011; Haugsrud, 2007; Lashtabeg *et al.*, 2010; Bevan *et al.*, 1982; Diot *et al.*, 2000; Ivanova *et al.*, 2012).

Here, we synthesize pure samples with a nominal composition of $La_{5.4}WO_{12-\delta}$ that show exceptional device performance and stability (Escolástico *et al.*, 2013). Complementary X-ray and neutron diffraction techniques are used to solve the average crystal structure, which goes beyond recently proposed models. We establish the structure of $La_{6-x}WO_{12-\delta}$, in particular lattice symmetry, degree of cation ordering and the location of oxygen vacancies. Real-space pair distribution function (PDF) analysis of high-energy synchrotron X-ray diffraction data is applied to confirm the model of the average crystal structure and to develop a model of the local crystal structure since total scattering analysis provides a tool to model Bragg and diffuse scattering simultaneously (Shoemaker *et al.*, 2010). EXAFS at the La *K* edge and W $L_3$ edge was performed to confirm the local crystal structure.

## 2. Experimental

### 2.1. Sample synthesis

The powder material was prepared using the corresponding anhydrous oxides as precursors. The reagents were milled in ethanol for 24 h, dried, calcined at 1073 K for 15h, and, after a second milling and drying step, calcined again at 1273 K for 15 h. Subsequently the mixture was milled again, pressed and then sintered at $T = 1673$ K. A stoichiometry of $La_{5.4}WO_{12-\delta}$ was selected to achieve phase-pure materials since nominal $La_6WO_{12}$ has been shown to contain $La_2O_3$ (Seeger *et al.*, 2013; Magrasó *et al.*, 2009).

### 2.2. Compositional analysis

Chemical composition was studied by neutron activation analysis (NAA) at the BERII reactor in Berlin and by inductively coupled plasma optical emission spectrometry (ICP-OES). Electron probe microanalysis (EPMA) using a JEOL JXA 8200 system was also applied. To increase the accuracy of the local composition analysis, the system was calibrated using elemental standards for tungsten and lanthanum phosphate.

### 2.3. Phase and structural analysis

Phase analysis was performed by applying X-ray diffraction using a Bruker D8 diffractometer in Bragg–Brentano geometry and Cu $K\alpha$ radiation. The crystal structure was studied in detail by different diffraction methods. High-resolution synchrotron X-ray powder diffraction (HRSXRPD) was performed at the ESRF beamline ID31 ($\lambda = 0.396$ Å, $T =$ 10 and 295 K) for 3 h per scan under progressive scaling of the counting time towards higher angles. Neutron powder diffraction (ND) data were collected on the D1A and D2B diffractometers at the Institut Laue–Langevin (ILL), Grenoble, at wavelengths of $\lambda = 1.909$ Å ($T = 300$–1173 K) and $\lambda = 1.595$ Å ($T = 298$ K), respectively. The D2B diffractometer was used in high-resolution mode with integration of the central part of the detector. Prior to all of the diffraction and EXAFS experiments the sample was dried for 96 h at 1173 K under an argon flow and loaded in a controlled helium atmosphere using a glove box. The combination of X-ray and neutron diffraction data proved to be crucial as the former is

sensitive to the heavy cations, while the neutron scattering lengths for W [4.86 (2) fm], La [8.24 (4) fm] and O [5.803 (4) fm] are comparable. Rietveld refinement of crystal structure models against the experimental data was performed using *GSAS* with the *EXPGUI* graphical user interface (Larson & Von Dreele, 2004; Toby, 2001). High-energy powder X-ray diffraction data were collected using ID15B also at the ESRF. The sample was contained in a glass capillary and an identical empty capillary was measured to estimate the experimental background. A wavelength of 0.1422 Å was used and the scattered X-rays were detected by a Mar345 image plate. The PDF was calculated using in-house software (*iPDF*) developed by one of the authors (SAJK), which runs as a graphical user interface within *Igor Pro* (https://www.wavemetrics.com/products/igorpro/igorpro.htm). Briefly, data were corrected for background, Compton scattering and the atomic form factor. The Compton shift, detector efficiency and incoherent fluorescence were also taken into account, before Fourier transformation according to

$$G(r) = \frac{2}{\pi}\int_0^\infty Q[S(Q)-1]\sin(Qr)\,\mathrm{d}Q. \quad (1)$$

$G(r)$ is the experimental atomic pair distribution function, $Q$ is the scattering vector magnitude, and $Q[S(Q)-1]$ represents the properly corrected and normalized intermediate structure factor. The $r$ grid used in real space had a spacing of 0.01 Å. Models were fitted to the PDF data using the *PDFgui* package (Farrow *et al.*, 2007). Model PDFs were calculated using

$$G(r) = \frac{1}{Nr}\sum_i \sum_{j\neq i}\left[\frac{f_i f_j}{\langle f\rangle^2}\,\delta(r-r_{ij})\right] - 4\pi r\rho_0. \quad (2)$$

The indices $i$ and $j$ run over all $N$ atoms in the sample. The scattering powers of the different atoms are $f_i$ and $f_j$, $\langle f\rangle$ is the average scattering power, $r$ represents the radial distance in real space, $r_{ij}$ is the distance between atoms $i$ and $j$, and $\rho_0$ is the number density. *PDFgui* uses the so-called small box approximation, which implies that the first summation above only runs over the atoms within one unit cell as defined by the average crystallographic structure. This approximation makes data modelling tractable out to relatively large distances in real space. Note that we approximate the scattering powers as the value of the X-ray form factor at $Q$ = 0. Because the $Q$ dependence of the form factor for heavy and light elements is considerably different, this has the potential to introduce errors in the calculated intensity of peaks which correspond to contacts between heavy (*i.e.* W) and light (*i.e.* O) atoms (Masson & Thomas, 2013). This error does not affect the peak positions. We justify this approximation for the present case by noting that the O atoms are practically invisible to X-ray scattering, contributing just 3% of the scattering for $La_{5.6}WO_{12-\delta}$. Therefore, the part of the PDF that has the largest error is also by far the smallest contribution. For La—W contacts, our approximation is reasonable, and for La—La or W—W contacts it is close to exact. We principally use the PDF to extract information on the displacements of the heavy atoms in this case, and the oxygen positions and metal coordination numbers are determined by complementary techniques.

### 2.4. EXAFS experiments

EXAFS was performed on beamline KMC-2 at BESSY II, Berlin, on the W $L_3$ absorption edge ($E$ = 10 207 eV) at room temperature and on beamline X at Hasylab, Hamburg, on the La $K$ absorption edge ($E$ = 38 925 eV) at 10 K. The measurements were performed in transmission mode, and the dried and ground sample was diluted in BN and pressed into pellets. The amount of two absorption lengths for the corresponding edges was used. The data were processed and analysed using the *IFEFFIT* code and the corresponding user interfaces *ATHENA* and *ARTEMIS* (Ravel & Newville, 2005). After background subtraction, the normalized and $k^3$-weighted spectra were Fourier transformed over a photoelectron wavenumber range of $k$ = 3.4–12.6 Å$^{-1}$ for the W $L_3$ edge and $k$ = 3.66–16.46 Å$^{-1}$ for the La $K$ edge. The theoretical EXAFS signal was calculated by performing *ab initio* calculations using the code *FEFF8.2* (Ankudinov *et al.*, 1998). The model was least-squares fitted to the data in $q$ space with the following fitting parameters: a single amplitude reduction factor $S_0^2$ and an overall energy parameter $\Delta E_0$ for each data set, fractional changes in bond length $\alpha$, and a mean-squared displacement parameter $\sigma^2$ for each coordination shell.

## 3. Results

### 3.1. Determination of the average crystal structure

**3.1.1. Initial steps.** The results of our NAA showed that the sample had a composition of $La_{5.4(2)}WO_{11.1}$. Analysis of the ICP-OES measurements gave a similar result. EPMA gave an La/W ratio of 5.57 (3). Our preliminary laboratory X-ray powder diffraction data showed that a doubled fluorite cell was found, with systematic absences consistent with face-

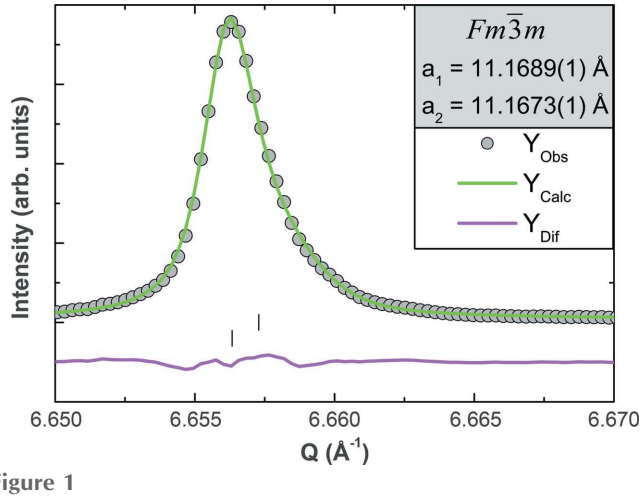


**Figure 1**
Observed, calculated and difference profiles for the Rietveld fit to the synchrotron X-ray diffraction profile of $La_{5.6}WO_{12-\delta}$, highlighting the region of the 10 6 2 reflection. The peak asymmetry is well fitted by the minimal broadening model discussed in the text.

**Table 1**
Results of Le Bail refinements to the D2B data at room temperature.

| Space group | Variables | $a$ (Å) | $b$ (Å) | $c$ (Å) | $\beta$ (°) | $V$ (Å$^3$) | $\chi^2$ | $R_p$ (%) | $wR_p$ |
|---|---|---|---|---|---|---|---|---|---|
| $Fm\bar{3}m$ | 7 | 11.1743 (1) | | | | 1395.3 (1) | 2.844 | 4.14 | 5.58 |
| $2 \times Fm\bar{3}m$ | 8 | 11.1736 (1) | | | | 1395.0 (1) | 2.056 | 3.55 | 4.74 |
| $I4/mmm$ | 8 | 7.9000 (1) | | 11.1795 (2) | | 697.7 (1) | 2.236 | 3.71 | 4.95 |
| $Immm$ | 9 | 7.9001 (1) | 7.8991 (2) | 11.1786 (2) | | 697.6 (1) | 2.258 | 3.73 | 4.97 |
| $C2/m$ | 10 | 11.1760 (2) | 11.1690 (3) | 7.9013 (1) | 134.96 (1) | 697.9 (1) | 2.153 | 3.65 | 4.85 |

centred cubic space groups. Because of the limited $Q$ range data and medium resolution of the laboratory X-ray diffraction data, the structure solution was performed using HRSXRPD. Trial Le Bail intensity extractions using the doubled fluorite unit cell resulted in poor fit statistics ($wR_P$ = 0.1214 and $\chi^2$ = 6.50) and close examination of the diffraction profile showed that this was caused by asymmetric peak broadening, which affected all reflections equally (Fig. 1). As various models have been proposed in the literature (Magrasó *et al.*, 2009, 2012, 2013), we performed an exhaustive search of distorted cells using Le Bail intensity extractions. This was compared with a minimal asymmetric broadening model which consisted of two cubic unit cells with an approximately 0.02% difference in lattice parameter [$a_1$ = 11.1689 (1), $a_2$ = 11.1673 (1) Å at 10 K with $wR_P$ = 0.0647 and $\chi^2$ = 2.82]. None of the distorted cells tested, including tetragonal ($I4/mmm$, No. 139), orthorhombic ($Immm$, No. 71) and monoclinic ($C2/m$, No. 12), gave better fit statistics than the phase separation model (Scherb, 2011). This result is significant because the lower-symmetry cells have more variables and so a higher degree of freedom in the intensity extractions. Note that ID31 is perhaps the highest-resolution powder diffractometer currently available, and that this tiny effect is invisible with other instrumentation. The D2B data collected in high-resolution mode could be well fitted with one cubic cell (see Table 1). The refined tetragonal cell shows a tetragonal distortion of $c/a(2^{1/2}) = 1.00065$. This small distortion of the cell allows us to describe the cell as cubic or pseudocubic.

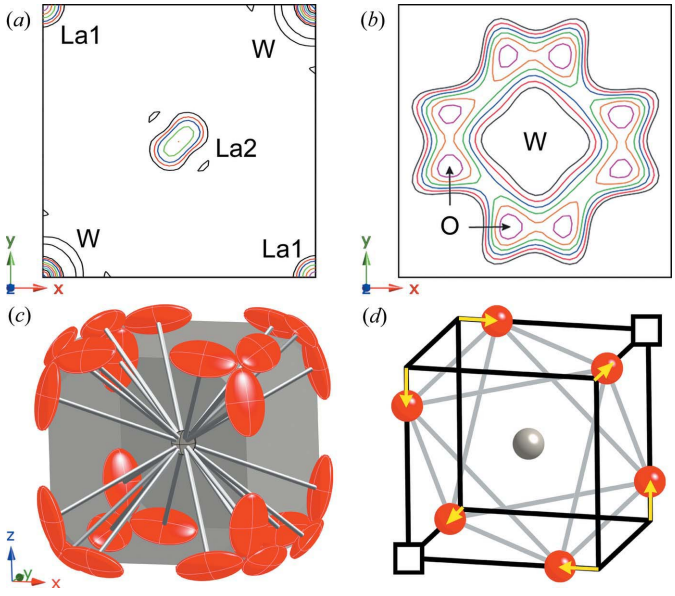


**Figure 2**
(*a*) Electron-density map calculated from HRSXRPD data collected at 10 K. The map size is one-half of the unit cell and the centre is at $x = y =$ 0.25 and $z = 0$. Contour lines with the same electron density are drawn at 1, 5, 10, 20, 30, 40, 50, 60, 70 and 80 Å$^{-3}$. (*b*) Fourier difference maps calculated from neutron powder diffraction data collected at 573 K, displaying the O site splitting around W. The map size is 4 × 4 Å and the centre is at $x = y = 0$ and $z$ = 0.125. Contour lines are drawn at 0.05, 0.10, 0.15, 0.20, 0.25 and 0.30 fm Å$^{-3}$. (*c*) Resulting model for the O site splitting around W (grey). The O split site (red) is shown with its anisotropic atomic displacement parameters at 573 K for 50% probability. (*d*) [111] oxygen vacancy pairs around W and the resulting oxygen displacements.

**3.1.2. Cation disorder**. Electron-density maps identified three heavy-atom positions, corresponding to the Wyckoff sites 4*a* (0, 0, 0), 4*b* ($\frac{1}{2}$, $\frac{1}{2}$, $\frac{1}{2}$) and 24*d* (0, $\frac{1}{4}$, $\frac{1}{4}$). These sites were attributed to the cations and, in the first cycles of Rietveld refinement, assumed to be statistically occupied with an La/W ratio of 5.6 as determined by EPMA. We initially assumed fluorite-type O sites [32*f* ($x, x, x$) position, $x_{O1} \simeq 0.125$ and $x_{O2} \simeq 0.375$]. After these initial steps, we then exploited the differing contrasts of the X-ray and neutron data sets to order the cations such that the 4*a* site with the highest electron density was occupied by W, the 4*b* site occupied by La, and the 24*d* site occupied with 96% La and 4% W. For the 24*d* site, the refined atomic displacement parameters were large and anisotropic. Our electron-density maps show that this site is actually split (Fig. 2*a*) into the 48*h* (0, $y, y$) site with 50% occupancy. These ∼0.22 Å displacements are static and localized as they were identical in the 10 and 295 K data sets. This disorder gave a much improved refinement and realistic atomic displacement parameters.

**3.1.3. Anion disorder**. Finally, we were able to develop a disordered model for the O sites coordinating the W 4*a* site. Difference Fourier maps were calculated from the neutron powder diffraction data (Fig. 2*b*). These showed that oxygen occupies the 96*k* site, with a total of 24 possible nearest neighbours arranged around the corners of a cube (Fig. 2*c*). The refined occupancy was found to be 24.3%, which is equivalent to an average coordination of 5.8 (1), as expected for octahedral $W^{6+}$. The oxygen displacement parameters were found to be anisotropic and elongated in the direction transverse to the W—O bonds. The local coordination can be explained by consideration of the defect chemistry. Assuming two vacancies per site, and that it is energetically favourable to locate them as far apart as possible, gives the picture shown in Fig. 2(*d*). The vacancy pair is located on one [111] axis of the cube. The nearest-neighbour anions can then relax towards

**Table 2**
Fractional atomic coordinates, occupancies and anisotropic displacement parameters $U_{ij}$ for $La_{5.6}WO_{12-\delta}$ at 298 K from neutron diffraction refined with space group $Fm\bar{3}m$.

Displacement parameters are multiplied by 100. The lattice parameter is $a$ = 11.1743 (1) Å and the residuals are $wR_P$ = 0.0547, $\chi^2$ = 2.752 and $R_{F^2}$ = 0.0264.

| Atom | Site | $x$ | $y$ | $z$ | $U_{eq}$ (Å$^2$) | Occupancy |
|---|---|---|---|---|---|---|
| W1 | 4*a* | 0 | 0 | 0 | 0.83 | 1.036 (21) |
| La1 | 4*b* | 0.5 | 0.5 | 0.5 | 1.16 | 1.013 (13) |
| La2 | 48*h* | 0 | 0.2357 (2) | 0.2357 (2) | 0.79 | 0.482 (6) |
| W2 | 48*h* | 0 | 0.2357 (2) | 0.2357 (2) | 0.79 | 0.018 (6) |
| O1 | 96*k* | 0.1120 (2) | 0.1120 (2) | 0.06456 (29) | 2.48 | 0.243 (4) |
| O2 | 32*f* | 0.3664 (1) | 0.3664 (1) | 0.36644 (10) | 1.84 | 0.969 (5) |

| Atom | $U_{11}$ (Å$^2$) | $U_{22}$ (Å$^2$) | $U_{33}$ (Å$^2$) | $U_{12}$ (Å$^2$) | $U_{13}$ (Å$^2$) | $U_{23}$ (Å$^2$) |
|---|---|---|---|---|---|---|
| W1 | 0.83 (14) | 0.83 (14) | 0.83 (14) | 0.00 | 0.00 | 0.00 |
| La1 | 1.16 (9) | 1.16 (9) | 1.16 (9) | 0.00 | 0.00 | 0.00 |
| La2 | 0.87 (9) | 0.75 (13) | 0.75 (13) | 0.00 | 0.00 | 0.16 (12) |
| W2 | 0.87 (9) | 0.75 (13) | 0.75 (13) | 0.00 | 0.00 | 0.16 (12) |
| O1 | 1.60 (18) | 1.60 (18) | 4.24 (25) | −0.34 (9) | −0.93 (11) | −0.93 (11) |
| O2 | 1.84 (4) | 1.84 (4) | 1.84 (4) | 0.17 (4) | 0.17 (4) | 0.17 (4) |

the defect in the [100] direction by 0.5 Å, forming a nearly regular octahedron. In combination with the cation disorder described above, this model then gave an excellent fit to both the synchrotron X-ray and neutron powder diffraction profiles (Fig. 3). The refined atomic coordinates, displacement parameters, occupancies and residuals from the fit to the latter are given in Table 2. In contrast to the model developed from Magrasó *et al.* (2013), the model developed here does not show negative mean-square atomic displacement parameters and physically impossible or unlikely atomic displacement parameters, especially for the W2 site.

If we consider full site occupation for the 4*a* and 4*b* sites, the refined composition of one unit cell is $La_{27.14}W_{4.86}O_{54.3}$ with an La/W ratio of 5.58 and 3.7 (1.3)% $W_{La2}$ anti-site defects on the split La2 site 48*h*. This is in excellent agreement with the results from EPMA. As a result of drying under argon at 1173 K prior to the diffraction experiments, additional oxygen vacancies are created and the colour of the sample changes

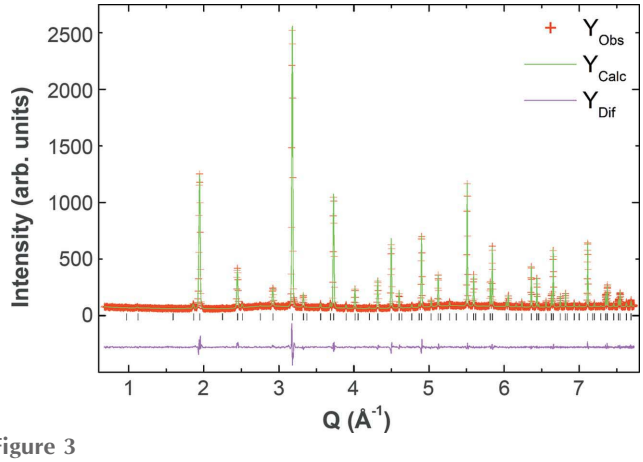


**Figure 3**
Observed, calculated and difference plots for the Rietveld fit to the high-resolution neutron powder diffraction data recorded at D2B at 298 K. The refined parameters are given in Table 2.

from white towards grey (Chang & Phillips, 1964). Therefore, the refined quantity of oxygen vacancies is too high for charge neutrality if we consider only $W^{6+}$ (54.3 O atoms per unit cell instead of 55.3). However, this discrepancy could be resolved if the $W_{La2}$ anti-site defect is reduced from $W^{6+}$ to $W^{4+}$ under reducing conditions during drying. The final model for the average crystal structure of $La_{5.6}WO_{12-\delta}$ is shown in Fig. 4. The structure is derived from a fluorite structure with doubled lattice parameter owing to cation ordering. The tungsten positions form a face-centred cubic (f.c.c.) lattice and nearest W neighbours are linked by the split La2 site, which has an average of sevenfold oxygen coordination. In the structural model developed here, around one La is replaced by W on the La2 site 48*h* to stabilize the $La_{5.6}WO_{12-\delta}$ phase. This is in complete contrast to $Ln_6WO_{12}$ materials containing rare earth atoms with small ionic radii, which show complete ordering of cations and oxygen vacancies (Diot *et al.*, 2000).

### 3.2. Local structure determination

**3.2.1. Development of the local model.** The model described in the previous section gives an excellent fit to the Bragg reflections of $La_{5.6}WO_{12-\delta}$. However, we detected strong diffuse scattering in the background of the neutron diffraction data sets (Fig. 5) which hints at local order. This oscillatory contribution is invisible to X-rays and hence probably originates from oxygen–oxygen correlations. To explain this signal, we returned to the defect model and considered how octahedral order might propagate through the lattice. As shown in Fig. 6, the orientation of a $WO_6$ octahedron influences that of its neighbours in a manner analogous to the way a magnetic exchange interaction links the orien-

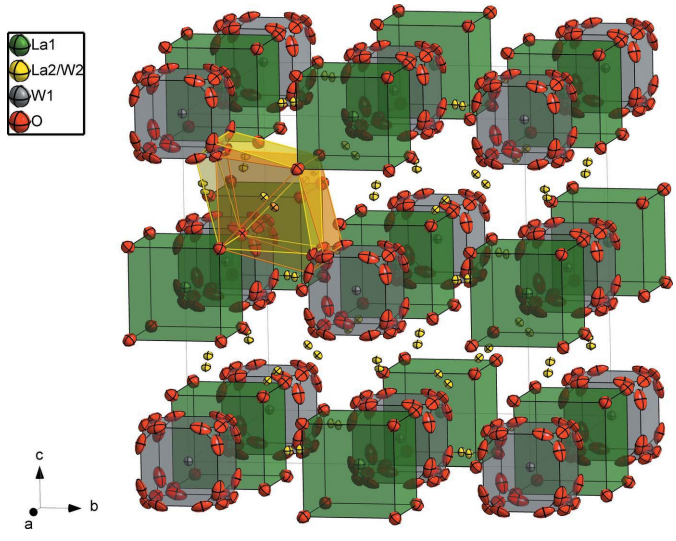


**Figure 4**
The average crystal structure refined for $La_{5.6}WO_{12-\delta}$ is shown with the anisotropic atomic displacement parameters at 298 K for 50% probability. Grey cubes represent W polyhedra with their partially occupied O sites (red), green cubes the La1 sites and yellow spheres the half-occupied La2 split sites. The two possible polyhedra for one La2 split site are shown in yellow and orange. About one out of 48 La2 positions is occupied by W, yielding the correct composition of $La_{5.6}WO_{12-\delta}$.

tation of localized spins in magnetic insulators. As described previously and shown in Fig. 2(*d*) and Fig. 6, removing the O atoms on one diagonal of a W polyhedron results in two oxygen vacancies and a relaxation of the remaining O atoms towards the vacancies to form a regular octahedron. The oxygen vacancies also reduce the coordination number of the neighbouring La2 site.

As sixfold coordination is energetically disfavoured for La (Greenwood & Earnshaw, 2003), this site then relaxes away from the defect towards the nearest-neighbour $WO_6$ octahedron. This model therefore explains why the La2 site is split along the line connecting two W sites. The possible orientations of the next $WO_6$ octahedron are then reduced, as shown in Fig. 6.

The importance of this novel 'chemical exchange interaction' is underlined by the simulation shown in Fig. 5. Here we calculated the powder averaged scattering $S(Q)$ of the dimer unit shown in the inset of Fig. 5 using the Debye equation, which assumes that the static approximation holds:

$$S(Q) \propto \frac{1}{N}\sum_i \sum_j b_i b_j \frac{\sin(Qr_{ij})}{Qr_{ij}}, \qquad (3)$$

where $b_i$ and $b_j$ are the neutron scattering lengths. This model reproduces the position of the maxima in the background and suggests that correlations between the orientation of $WO_6$ octahedra extend beyond at least one shell.

**3.2.2. PDF analysis.** As the above modelling of the diffuse scattering is only qualitative, we compared the average and local structures with the X-ray PDF of $La_{5.6}WO_{12-\delta}$ at room temperature. While the X-ray PDF is not especially sensitive to the position of the O atoms, it is highly sensitive to the displacements of the La2 sites as we describe in more detail below. The so-called intermediate structure factor, $Q[S(Q)-1]$, of $La_{5.6}WO_{12-\delta}$ is shown in Fig. 7(*a*). The signal is seen to be damped to near zero above $Q = 15$ Å$^{-1}$ as a result of disorder. We truncated this data set at $Q = 24$ Å$^{-1}$ and performed the Fourier transformation described in §2. This yields the PDF shown in Fig. 7(*b*). In order to determine the length scale of the local order, we performed refinements of two structures against this data set in the range $1.5 < r < 12$ Å.

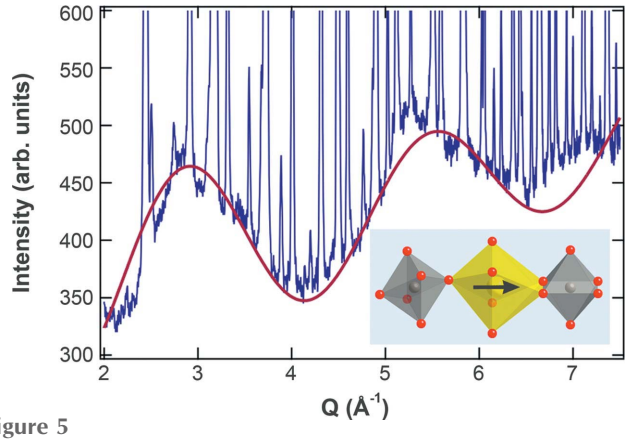


**Figure 5**
Diffuse scattering of neutrons is observed at room temperature for dry samples of $La_{5.6}WO_{12-\delta}$. The red line is a calculation of scattering from local order over the pair of sites shown in the inset using equation (3) and a background $\propto Q^2$ to account for phonon scattering. Note that the sample was contained in a vanadium can for this measurement. This sample container only contributes a structureless incoherent background to this data set.

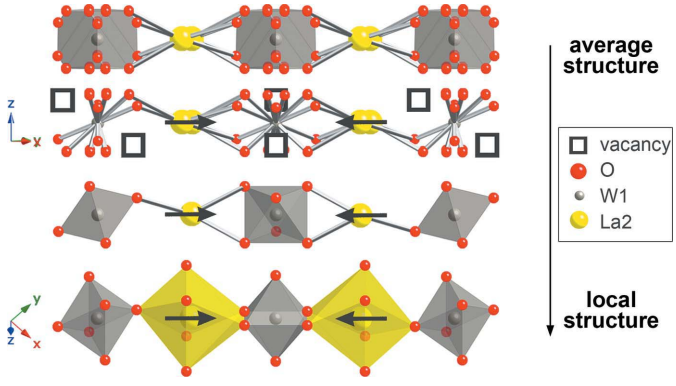


**Figure 6**
Development of a possible local configuration (bottom) from the average crystal structure (top) with La and O split sites. Fixing the orientation of a single $WO_6$ octahedron propagates order to nearest neighbours. To preserve an La coordination of seven, La must share one oxygen defect, resulting in a displacement of La as shown by arrows.

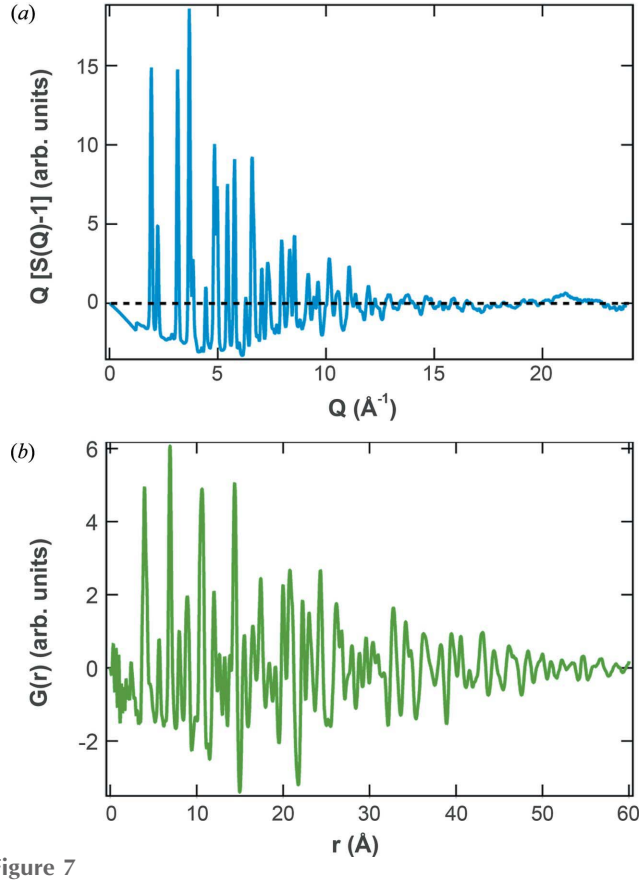


**Figure 7**
(*a*) Corrected intermediate structure factor, $Q[S(Q)-1]$, for $La_{5.6}WO_{12-\delta}$, calculated from the high-energy powder diffraction data as described in the text. (*b*) PDF for $La_{5.6}WO_{12-\delta}$ calculated in the range $0 < r < 60$ Å by Fourier transformation of the data shown in (*a*). The *r* grid used was 0.01 Å.

Models were fitted in the small box approximation described in §2 and the calculated PDF was convoluted with the Fourier transform of the box function representing the measured $Q$ range. Isotropic atomic displacement parameters were used and we applied a sharpening correction for correlated motion in the first coordination sphere. The observed damping of the PDF in real space (which is due to the instrumental resolution) was accounted for by measuring a standard ($CeO_2$, NIST674b).

The first structure we refined against the data was the average $Fm\bar{3}m$ structure determined above. This fitted well ($R_w$ = 0.0955), but with some misfits in the first coordination shell [see the peak at ∼2 Å in Fig. 8(*a*)]. We therefore generated a new structure in $Pa\bar{3}$, which consisted of ordered $WO_6$ octahedra and La displacements, as shown in Fig. 6. Despite the fact that this structure does not model any of the average structure displacements of La or O atoms, it not only provides a better fit ($R_w$ = 0.0876), but also gives a chemically reasonable W—O bond length of 1.87 Å. The corresponding sharp peak in the PDF (Fig. 8*b*) reflects the strongly covalent nature of these bonds and validates the earlier assumptions about octahedral coordination. The local coordination units in $La_{5.6}WO_{12-\delta}$ can therefore be regarded as rigid bodies, rather than the highly distorted and disordered units inferred from the average structure.The refined coordinates from this model are given in Table 3 and the final local crystal structure is shown in Fig. 9.

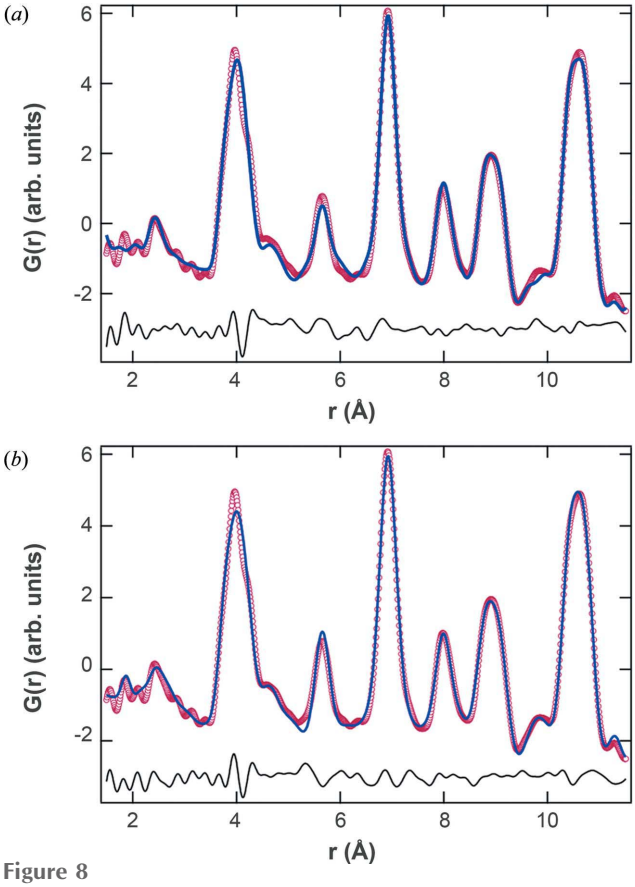


**Figure 8**
Observed, calculated and difference plots for the real-space fits to the X-ray PDF of $La_{5.6}WO_{12-\delta}$ at room temperature. In (*a*) the fit to the average structure in $Fm\bar{3}m$ is shown and in (*b*) the fit to the local structure in $Pa\bar{3}$ is shown.

**Table 3**
Refined atomic coordinates for $La_{5.6}WO_{12-\delta}$ at room temperature from synchrotron X-ray PDF analysis in space group $Pa\bar{3}$.

The lattice parameter $a$ = 11.299 Å. Site occupancies are unity and displacement parameters are multiplied by 100. Note that errors are not properly propagated by the software used to radially integrate two-dimensional detector images. Nevertheless, directly fitting Gaussian functions to peaks in $G(r)$ yields error bars similar to those extracted by Rietveld refinement. This does not affect the validity of our comparison between the $Fm\bar{3}m$ and $Pa\bar{3}$ models shown in Fig. 9. The bond distances which result from the coordinates listed below are also highly consistent with those extracted by our EXAFS experiments (Fig. 12).

| Atom | Site | $x$ | $y$ | $z$ | $U_{iso}$ (Å$^2$) |
|---|---|---|---|---|---|
| W1 | 4*a* | 0 | 0 | 0 | 0.96 |
| La1 | 4*b* | 0.5 | 0.5 | 0.5 | 1.36 |
| La2/W2 | 24*d* | 0.999 | 0.2634 | 0.2633 | 1.36/0.96 |
| O1 | 24*d* | 0.9209 | 0.8699 | 0.0654 | 2.39 |
| O2 | 8*c* | 0.6222 | 0.6222 | 0.6222 | 2.39 |
| O3 | 24*d* | 0.6567 | 0.3606 | 0.3742 | 2.39 |

While both models give good fits to the PDF data up to ∼10 Å, we found that the fit of the average model was better at longer distances. This effect arises because different $r$ ranges of the PDF are sensitive to order on different length scales. We therefore performed a series of structure refinements where the fitted maximum ($r_{max}$) was increased in a stepwise fashion. We could then compare the residual values for the two models and estimate the length scale of the local order in $La_{5.6}WO_{12-\delta}$. The results of this analysis are shown in Fig. 10. The difference $R_w$(local) − $R_w$(average) is negative until $r_{max}$ exceeds 35 Å. When data at longer distances are included, the average structure determined by Bragg diffraction becomes more favourable. It should be noted that the

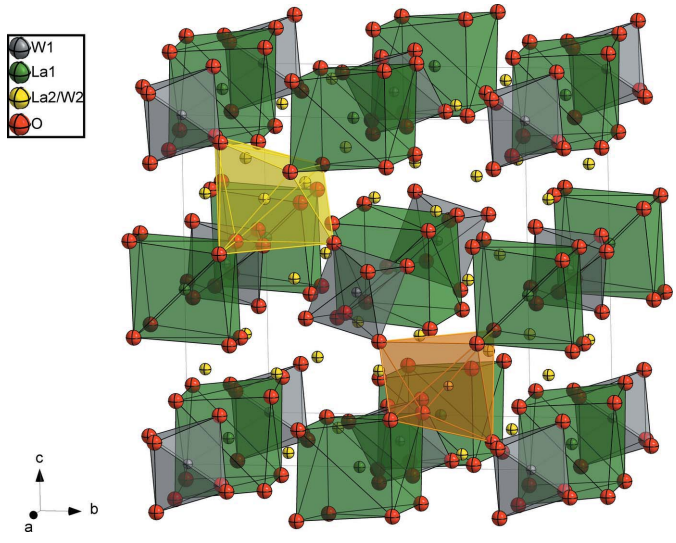


**Figure 9**
Local crystal structure for $La_{5.6}WO_{12-\delta}$ in space group $Pa\bar{3}$ (No. 205) shown with the isotropic atomic displacement parameters at 298 K for 50% probability. Red spheres represent O atoms, grey W octahedra, green cubes La1 sites and yellow spheres La2 sites. One out of 24 La2 positions is occupied by W (orange), ensuring the correct composition $La_{5.6}WO_{12-\delta}$.

refined $Pa\bar{3}$ structure completely failed to describe the data sets shown in Fig. 3 when we attempted Rietveld refinements. This confirms that the length scale for the order in $La_{5.6}WO_{12-\delta}$ is restricted to small domains of the order of 3.5 nm, which is well below the coherence length required to yield sharp Bragg reflections. We note that our analysis provides no information on the shape or orientation of these domains as our model assumes uncorrelated spherical regions.

**3.2.3. EXAFS.** In order to provide an element-specific confirmation of our proposed local structure, we turn now to the results of our EXAFS experiments on the W $L_3$ and La $K$ edges. The former also provided confirmation of the small amount of anti-site disorder on the La2 sites, which is close to the minimum measurable by diffraction techniques. Both of the data sets provided information out to ~6 Å as shown in Fig. 10. Fitting of the models to the data was performed in $q$ space. As a starting model we used the $Pa\bar{3}$ structure refined against the PDF data above. For both edges, the shells were fitted in $q$ space one after another, and as a final step all shells were fitted together.

At the W $L_3$ edge, we compared two different variations on the $Pa\bar{3}$ structure. The first model with a nominal La/W ratio of 7 (four W per unit cell) contains only one W site at 4*a*. This refinement gave a rather poor $R$ factor of 3%. However, a dramatic improvement was observed when anti-site disorder was considered in the second model. This model contains two W sites and had a nominal La/W ratio of 5.4 (five W per unit cell). Four W were placed on the 4*a* site and one additional W was substituted onto the La2 24*d* site. This fit gave a dramatically improved $R$ factor of 0.3%. The Fourier transformed and $k^3$-weighted EXAFS data, together with the best-fit line from this model, are shown in Figs. 11(*a*) and 11(*c*). The second W site is manifested by the W–La/W peak at 2.8 Å, as well as the W—La/W distance at 3.5 Å. Note that these data are not phase corrected and the fitted bond lengths are given in Table 4.

For refinements against the La $K$ edge EXAFS data, we used the same structural model as developed above. This model contains 27 La atoms on two La sites, four La on site 4*b* and 23 La on site 24*d*. The refinement was performed with all scattering paths for the two La sites up to 5.6 Å (36 paths for two La sites). Once again, we achieved excellent agreement between the data and the model calculation, with an $R$ factor of 0.15%. The Fourier transformed and $k^3$-weighted EXAFS data, together with the best-fit line from this model, are shown in Figs. 11(*b*) and 11(*d*). The bond lengths extracted from this refinement are given in Table 4. In the final structure, the La1 site has a highly regular environment of 7.8 (3) O ions arranged on the corners of a cube and 12 La neighbours. The surroundings of the La2 site, however, show a high degree of disorder. La2 is sevenfold coordinated by O and the bond distances are between 2.38 and 2.67 Å. The second coordination shell comprises 12 metal neighbours and is split into seven subshells between 3.66 and 4.20 Å. Because of the disorder of the second shell, the metal–metal peak shown in Fig. 11(*b*) at 3.5 Å is very broad and the signal is strongly damped at higher radial distances. Nevertheless, as our model describes the local structure well, the Debye–Waller factors remain small, showing no contribution from un-modelled static disorder.

A comparison of the results of fitting the W $L_3$ and La $K$ edges shows how the anion sublattice relaxes around the W anti-site defects. For example, we find a contraction of the metal–oxygen distance in the first coordination shell when $La^{3+}$ is replaced by the smaller and more highly charged $W^{6+}$ cations. Indeed, the shortest bonds from the 24*d* site are reduced from 2.380 (5) to 1.839 (16) Å. The latter value is in excellent agreement with the W—O distance extracted for the

**Table 4**
Refined bond distances, coordination numbers (CN) and Debye–Waller factors from fitting of the La $K$ edge (10 K) and W $L_3$ edge (295 K) EXAFS signal of $La_{5.6}WO_{12-\delta}$ (the $Pa\bar{3}$ local structure model was used as a starting point).

W $L_3$ edge: $R$ = 0.00329, $S_0^2$ = 0.87 (3), $\Delta E_0$ = −0.27 (19). La $K$ edge: $R$ = 0.00148, $S_0^2$ = 0.73 (6), $\Delta E_0$ = 4.8 (8).

| | | First shell | | | Second shell | | | |
|---|---|---|---|---|---|---|---|---|
| Atom | Site | $d_{W/La\text{-}O}$ (Å) | CN | $\sigma^2$ (Å$^2$) | $d_{W/La\text{-}M$ (Å) | $M$ | CN | $\sigma^2$ (Å$^2$) |
| W1 | 4*a* | 1.908 (2) | 6 | 0.003 (1) | 3.687 (5) | La | 6 | 0.011 (1) |
| | | | | | 4.136 (7) | La | 6 | 0.011 (1) |
| W2 | 24*d* | 1.839 (16) | 2 | 0.005 (1) | 3.199 (13) | W | 1 | 0.009 (4) |
| | | 1.871 (16) | 2 | 0.005 (1) | 3.199 (13) | La | 2 | 0.005 (1) |
| | | 2.25 (4) | 1 | 0.005 (1) | 3.363 (14) | La | 2 | 0.005 (1) |
| | | 2.36 (5) | 1 | 0.005 (1) | 3.391 (14) | La | 2 | 0.005 (1) |
| | | 2.39 (5) | 1 | 0.005 (1) | 3.413 (15) | La | 2 | 0.005 (1) |
| | | | | | 3.583 (15) | W | 1 | 0.009 (4) |
| | | | | | 3.621 (15) | La | 2 | 0.005 (1) |
| La1 | 4*b* | 2.540 (8) | 7.8 (3) | 0.002 (1) | 3.973 (22) | La | 12 | 0.0055 (23) |
| La2 | 24*d* | 2.380 (5) | 2 | 0.0026 (3) | 3.655 (10) | W | 1 | 0.0034 (4) |
| | | 2.421 (5) | 2 | 0.0026 (3) | 3.755 (7) | La | 2 | 0.0060 (8) |
| | | 2.513 (12) | 1 | 0.0032 (7) | 3.947 (8) | La | 2 | 0.0060 (8) |
| | | 2.643 (12) | 1 | 0.0032 (7) | 3.955 (8) | La | 2 | 0.0060 (8) |
| | | 2.671 (12) | 1 | 0.0032 (7) | 3.980 (8) | La | 2 | 0.0060 (8) |
| | | | | | 4.082 (11) | W | 1 | 0.0034 (4) |
| | | | | | 4.195 (14) | La | 2 | 0.0060 (8) |

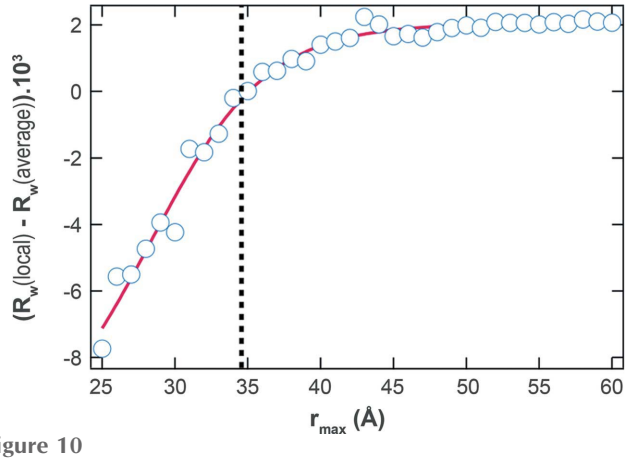


**Figure 10**
The local structure model describes the PDF of $La_{5.6}WO_{12-\delta}$ better than the average structure model up to distances of 35 Å. The plot shows the difference between the residuals of the two models as a function of the maximum $r$ value fitted.

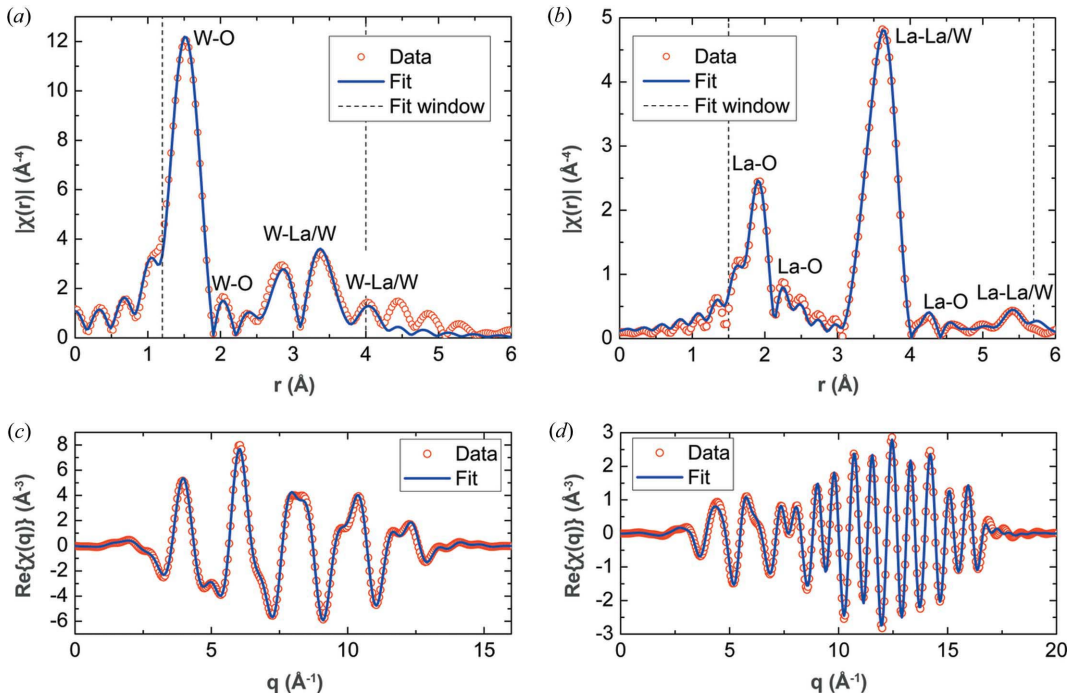


**Figure 11**
Fourier transformed $k^3$-weighted EXAFS data as a function of the radial distance (uncorrected for phase shifts) together with the fit and the fitting window are shown for (*a*) the W $L_3$ edge at 295 K and (*b*) the La *K* edge at 10 K. The fits were performed in *q* space (*c*) and (*d*) for the local crystal structure in $Pa\bar{3}$ (see Fig. 9).

fully occupied 4*a* site [1.908 (2) Å], as well as that found by our PDF experiments (1.87 Å). Our EXAFS results therefore fully support the local structure we developed for $La_{5.6}WO_{12-\delta}$ by diffraction measurements and confirm the presence of the ∼4% anti-site disorder on the La2 site.

A direct comparison of the bond lengths obtained by refining the $Pa\bar{3}$ structure against the EXAFS and PDF data sets is shown in Fig. 12. We find a linear relationship for all the bond lengths. For those distances that include O atoms, the spread is notably worse, which might reflect the approximations made in equation (2) while modelling the PDF data. Nevertheless, the overall agreement between the two techniques is remarkable, and we find a correlation coefficient of 0.9924 by fitting a straight line which passes through the origin. This analysis is the final confirmation of the local structure model which we have developed.

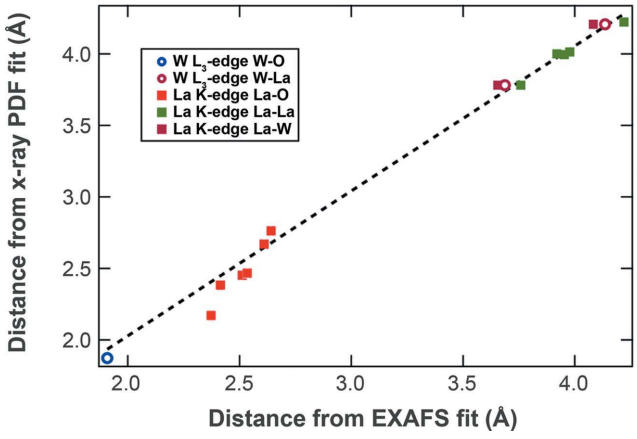


**Figure 12**
Plot of the bond lengths in $La_{5.6}WO_{12-\delta}$ obtained by fits to the EXAFS data *versus* those obtained by fits to the PDF data. A line which passes through the origin was fitted to the data, resulting in an extracted Pearson correlation coefficient of 0.9924. Error bars from the EXAFS fitting are smaller than the symbol size. See the caption to Table 3 for a discussion of the errors from fitting the PDF data. Note that the correlation between PDF and EXAFS measurements is the result of three different experiments, performed at three different synchrotrons.

## 4. Discussion

The above experiments have identified a complex hierarchy of structure, which spans multiple length scales in $La_{5.6}WO_{12-\delta}$. In what follows, we briefly review our average structure in comparison to earlier work and discuss the local structure in more detail. The lattice symmetry of $La_{5.6}WO_{12-\delta}$ has previously been called into question on the basis of very high resolution synchrotron X-ray powder diffraction experiments performed at the ESRF (Magrasó *et al.*, 2012). However, our results show that $La_{5.6}WO_{12-\delta}$ is actually cubic, but with slightly asymmetric peak broadening that implies a tiny (∼0.02%) lattice parameter distribution. We emphasize again that this effect is masked entirely by the resolution of standard X-ray and neutron diffraction instrumentation. This small peak broadening can be explained in terms of a lattice parameter spread caused by incomplete diffusion of the reactants and the resulting slightly different local compositions and/or vacancy concentrations. Having accounted for this effect, we were able to propose a new average structure model in space group $Fm\bar{3}m$, which has three improvements on previously

published work. Firstly, we identified positional disorder on parts of the metal sublattice, which has an appealing explanation in terms of the defect chemistry in $La_{5.6}WO_{12-\delta}$. We find (Fig. 2*a*) that the La2 site is split into two 50:50 occupied sites with displacement along the vectors joining neighbouring W sites. When the possible location of oxygen vacancies in the lattice (Figs. 2 and 6) is accounted for, this finds a natural explanation, as the La sites relax away from the defects to maintain sevenfold coordination. As we discuss more fully below, this is naively expected to propagate order through the lattice at temperatures below the onset of oxygen ion conduction. Secondly, the split model for the La2 and O1 sites developed here does not show any negative atomic displacement parameters, and the static contribution to the atomic displacement parameters is reduced. The third improvement of our model on previous work is the quantification of anti-site disorder. The possibility of a small amount (*ca* 5%) of W substitution on the La2 sites was suggested from DFT calculations. However, no direct evidence of this has yet been presented. Here we used a combination of X-ray and neutron diffraction, and exploited the differing contrasts of these techniques to get a consistent estimate of the anti-site disorder. When we refined the occupancy of the La2 site against the X-ray data, it rose to above unity, consistent with a small amount of heavier W. Indeed, the refined X-ray scattering power was equivalent to 53.0 $e^-$, where $f_1(La^{3+})$ = 52.5 $e^-$ and $f_1(W^{6+})$ = 67.3 $e^-$ for X-rays with an energy of 31.3 keV. For the refinement against the neutron diffraction data, we found an average scattering length of 8.108 fm, reduced from the value expected for La ($b_{coh}$ = 8.24 fm), again consistent with substitution by W ($b_{coh}$ = 4.86 fm). These measurements thus enabled us to calculate an anti-site disorder of 3.7 (1.3)%. In addition, EXAFS measurements on the W $L_3$ edge, which are much more sensitive to this small structural perturbation, gave an additional confirmation. The unique element specificity of EXAFS means that extra sites are immediately apparent. Here we found an order of magnitude decrease in the fitting residuals of our structure refinement when we included the trace amount of anti-site disorder inferred from the diffraction measurements.

While the details described above complete the description of the average structure of $La_{5.6}WO_{12-\delta}$, our results go much further on local length scales. We were able to obtain qualitative insight into the local structure by using simple chemical concepts. For example, from an electrostatic point of view, the approximately octahedral coordination of W shown in Fig. 2(*d*) is by far the most likely as it minimizes the repulsion between ligands. Similar effects have been inferred for other simple functional materials, such as scandium- and yttrium-stabilized zirconias (Steele & Fender, 1974; Irvine *et al.*, 2007). This is shown by diffuse scattering observed in neutron powder diffraction experiments which are sensitive to oxygen order. Here, a simple model of two linked octahedra accounts for the peak positions of this scattering (Fig. 5). This result suggests the intriguing possibility that order might propagate over a limited range, below the coherence length required to produce sharp Bragg peaks. Assuming that all octahedra have fixed orientations produces our $Pa\bar{3}$ structure (Fig. 9). Once again, this insight from diffraction is strongly supported by our EXAFS data sets, which were also satisfactorily fitted by this model.

If we compare the local structure in $Pa\bar{3}$ with the bixbyite structure of the reactant $La_2O_3$ in space group $Ia\bar{3}$ (*C*-type) some similarities can be seen. The body centring is lost owing to an ordered arrangement of the cations La and W ($Ia\bar{3}$: 8*a* La1 → $Pa\bar{3}$: 4*a* W1 and 4*b* La1). However, the coordination of La1 in $La_2O_3$ is octahedral and the oxygen vacancies sit on the diagonal of the cube surrounding La1, which results in a relaxation of the remaining O atoms in the direction of the vacancies. This is very similar to the $WO_6$ octahedra in $La_{5.6}WO_{12-\delta}$ (see Fig. 2*d*). For $La_2O_3$ the La2 site is displaced from $(0, \frac{1}{4}, \frac{1}{4})$ in the direction of the edge-shared $LaO_6$ octahedra, which is exactly the same in the local structure developed here where the La2 site relaxes in the direction of the edge-shared $WO_6$ octahedron (see Figs. 6 and 13). This results in two different W1—La2 bond lengths which are compared in Table 5 for the different methods used. The extracted differences in bond length match with the difference in La1—La2 bond length for $La_2O_3$ which is 0.46 Å. In contrast to $La_2O_3$, for $La_{5.6}WO_{12-\delta}$ the symmetry of the local structure is broken owing to oxygen vacancies, which result in different orientations of $WO_6$ octahedra and La2 displacements or the $W_{La2}$ anti-site defects. This prevents the local structure from establishing long-range order.

We completed our picture of the local structure using real-space refinements against our X-ray PDF data. This provides a definitive model for the $Pa\bar{3}$ structure which will be of significant use for DFT investigations of the mechanism for mixed conduction. Furthermore, since we were able to Fourier transform our data out to at least 60 Å, we could estimate the size of the coherent $Pa\bar{3}$ domains. This analysis yielded a local

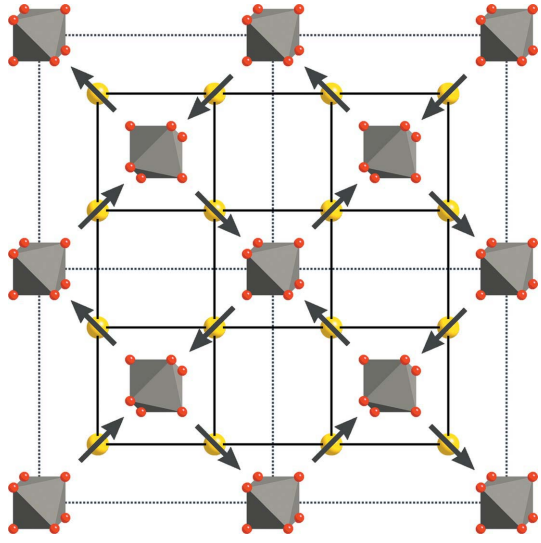

**Figure 13**
The f.c.c. lattice of W octahedra (grey) and the medial lattice (black) are shown according to the Ising model. The arrows display the 'Ising spins' on the medial lattice indicating La2 atoms (yellow) displaced into or away from $WO_6$ sites. The La1 site 4*b* is not shown for clarity.

**Table 5**
Comparison of splitting of the La2 site for different methods and temperatures.

Rietveld refinements of the HRSXRPD and neutron diffraction patterns were performed with the average crystal structure in space group $Fm\bar{3}m$ with the half-occupied split site La2. For PDF and EXAFS measurements, where the local crystal structure in space group $Pa\bar{3}$ was used for the refinements, the distance was calculated using the two different W1—La2 bond lengths.

| Method | Instrument | $T$ (K) | $\Delta d_{\mathrm{W1\text{-}La2}}$ (Å) |
|---|---|---|---|
| HRSXRPD | ID31 (ESRF) | 10 | 0.45 (1) |
| | ID31 (ESRF) | 295 | 0.44 (1) |
| ND | D2B (ILL) | 298 | 0.45 (1) |
| | D1A (ILL) | 573 | 0.44 (1) |
| | D1A (ILL) | 1073 | 0.43 (1) |
| PDF | ID15b (ESRF) | 295 | 0.43 (1) |
| EXAFS | | | |
| La $K$ edge | Beamline X (Hasylab) | 10 | 0.43 (2) |
| W $L_3$ edge | KMC-2 (BESSY II) | 295 | 0.45 (1) |

coherence length of *ca* 3.5 nm. Therefore, the ordered local structure is only stable for a domain size of a few unit cells. In contrast, the average structural model contains all possibilities of distorted and tilted $WO_6$ octahedra and La displacements and is valid for the whole material. Such a behaviour of defective fluorite-type phases was previously described for stabilized zirconia, which contains microdomains of about 30 Å in diameter embedded coherently in a number of specific orientations within a cubic matrix (Allpress & Rossell, 1975). In addition, the electrical properties of the material are closely related to their crystal structure. In this case, complete ordering of anion vacancies is less favourable for the anion mobility (García-Martín *et al.*, 2005). We anticipate that future PDF experiments performed at high temperatures will enable determination of the link between this length scale and mixed conduction performance in $La_{5.6}WO_{12-\delta}$.

Finally, the observation of local order over a limited length scale raises interesting questions. For example, why is this high-entropy ground state favoured in $La_{5.6}WO_{12-\delta}$? Furthermore, what factors prevent long-range order from establishing itself in this material? We conclude our discussion by briefly speculating about connections with a seemingly unrelated field, that of so-called frustrated materials (Henley, 2010; Bramwell & Gingras, 2001). These are materials in which pairwise interactions (for example, an antiferromagnetic exchange interaction, $J$) compete because of the lattice connectivity. Long-range order is not established even at temperatures where $k_B \ll J$ ($k_B$ is the Boltzmann constant). The canonical example is water ice, where local rules enforcing the formation of bent water molecules create a massively degenerate ground-state manifold. Here the picture is similar. In our local structure, the W cations are placed on a non-bipartite f.c.c. lattice (see Fig. 13). When pairwise interactions are present (such as our local rule linking the orientation of $WO_6$ octahedra) this lattice is frustrated. We speculate that this also results in a hugely degenerate number of structures for $La_{5.6}WO_{12-\delta}$, which results in the 'glassy' ground state we observe.

Indeed, our average structure model is nothing more than the result of spatially averaging the orientation of all of the $WO_6$ octahedra and La2 displacements in the sample. We note, in passing, that much as the proton displacements in water ice map to an Ising spin model ('spin ice') (Castro Neto *et al.*, 2006), the La displacements in $La_{5.6}WO_{12-\delta}$ map to a well studied Ising model of the octahedral lattice (Henley, 2010). This comparison may be relevant for future investigations of defect dynamics in $La_{5.6}WO_{12-\delta}$. For example, the propagation of defects in frustrated models is often quite different from that in standard materials. For example, protons diffuse through ice (Castro Neto *et al.*, 2006), rather than the hopping motion found in ceramic proton conductors (Karlsson *et al.*, 2009). We believe future investigations of the local interactions in $La_{5.6}WO_{12-\delta}$ and other ionic conductors are thus well merited and speculate that so-called 'function through frustration' may be an appealing route to designing new ionic conductors in the future.

## 5. Conclusions

In summary, we have reported a detailed study of both the average and the local structure of $La_{5.6}WO_{12-\delta}$. We show that the former has both positional and substitutional disorder of metal sites, as well as partially occupied anion sites. However, our diffuse scattering experiments show that, on a local scale, rigid $WO_6$ octahedra are found and we propose a simple defect rule which links the orientation of neighbouring sites. Our local structure is confirmed by EXAFS experiments and will be of significant use in further modelling the mixed conduction of this class-leading material.

## Acknowledgements

We thank the Helmholtz Association for funding through the Helmholtz Alliance MEM-BRAIN (Initiative and Networking Fund) and the Spanish government (grant No. ENE2011-24761). We thank D. Alber and G. Bukalis for NAA measurements and E. Suard and G. Nenert for assistance with neutron diffraction data collection. The European Synchrotron Radiation Facility, BESSY-II, Hasylab and the Institut Laue–Langevin are thanked for the provision of beamtime. We thank S. J. L. Billinge, A. Fantin, T. Fennell, D. J. P. Morris, J. K. Rana and D. A. Tennant for useful discussions.

## References

Allpress, J. & Rossell, H. (1975). *J. Solid State Chem.* **15**, 68–78.
Ankudinov, A. L., Ravel, B., Rehr, J. J. & Conradson, S. D. (1998). *Phys. Rev. B*, **58**, 7565–7576.
Aricò, A. S., Bruce, P., Scrosati, B., Tarascon, J.-M. & van Schalkwijk, W. (2005). *Nat. Mater.* **4**, 366–377.
Bevan, D. J. M., Drennan, J. & Rossell, H. J. (1982). *Acta Cryst.* B**38**, 2991–2997.
Bramwell, S. T. & Gingras, M. J. P. (2001). *Science*, **294**, 1495–1501.
Castro Neto, A. H., Pujol, P. & Fradkin, E. (2006). *Phys. Rev. B*, **74**, 024302.
Chang, L. L. Y. & Phillips, B. (1964). *Inorg. Chem.* **3**, 1792–1794.
Diot, N., Bénard-Rocherullé, P. & Marchand, R. (2000). *Powder Diffr.* **15**, 220–226.
Escolástico, S., Solís, C., Scherb, T., Schumacher, G. & Serra, J. M. (2013). *J. Membr. Sci.* **444**, 276–284.

Escolástico, S., Vert, V. B. & Serra, J. M. (2009). *Chem. Mater.* **21**, 3079–3089.
Fabbri, E., Pergolesi, D. & Traversa, E. (2010). *Chem. Soc. Rev.* **39**, 4355–4369.
Farrow, C. L., Juhas, P., Liu, J. W., Bryndin, D., Božin, E. S., Bloch, J., Proffen, T. & Billinge, S. J. L. (2007). *J. Phys. Condens. Matter*, **19**, 335219.
Fontaine, M. L., Larring, Y., Norby, T., Grande, T. & Bredesen, R. (2007). *Ann. Chim. Sci. Mat.* **32**, 197–212.
García-Martín, S., Alario-Franco, M. A., Fagg, D. P. & Irvine, J. T. S. (2005). *J. Mater. Chem.* **15**, 1903–1907.
Greenwood, N. N. & Earnshaw, A. (2003). *Chemistry of the Elements*, 2nd ed. Oxford, Boston: Butterworth–Heinemann.
Haugsrud, R. (2007). *Solid State Ionics*, **178**, 555–560.
Hempelmann, R., Soetratmo, M., Hartmann, O. & Wappling, R. (1998). *Solid State Ionics*, **107**, 269–280.
Henley, C. L. (2010). *Annu. Rev. Condens. Matter Phys.* **1**, 179–210.
Irvine, J. T. S., Dobson, J. W. L., Politova, T., García Martín, S. & Shenouda, A. (2007). *Faraday Discuss.* **134**, 41–49.
Ivanova, M., Seeger, J., Serra, J., Solis, C., Meulenberg, W., Fischer, W., Roitsch, S. & Buchkremer, H. (2012). *Chem. Mater. Res.* **2**, 56–81.
Jordal, K., Bredesen, R., Kvamsdal, H. M. & Bolland, O. (2004). *Energy*, **29**, 1269–1278.
Kalland, L.-E., Magrasó, A., Mancini, A., Tealdi, C. & Malavasi, L. (2013). *Chem. Mater.* **25**, 2378–2384.
Karlsson, M., Matic, A., Engberg, D., Björketun, M. E., Koza, M. M., Ahmed, I., Wahnström, G., Börjesson, L. & Eriksson, S.-G. (2009). *Solid State Ionics*, **180**, 22–28.
Kreuer, K. D. (2003). *Annu. Rev. Mater. Res.* **33**, 333–359.
Larson, A. C. & Von Dreele, R. B. (2004). *GSAS*. Report LAUR 86–748. Los Alamos National Laboratory, New Mexico, USA.
Lashtabeg, A., Bradley, J., Dicks, A., Auchterlonie, G. & Drennan, J. (2010). *J. Solid State Chem.* **183**, 1095–1101.
Li, L., Borry, R. W. & Iglesia, E. (2002). *Chem. Eng. Sci.* **57**, 4595–4604.
Magrasó, A., Frontera, C., Marrero-López, D. & Núñez, P. (2009). *Dalton Trans.* pp. 10273–10283.
Magrasó, A. & Haugsrud, R. (2014). *J. Mater. Chem. A*, **2**, 12630–12641.
Magrasó, A., Hervoches, C. H., Ahmed, I., Hull, S., Nordström, J., Skilbred, A. W. B. & Haugsrud, R. (2013). *J. Mater. Chem. A*, **1**, 3774–3782.
Magrasó, A., Polfus, J. M., Frontera, C., Canales-Vázquez, J., Kalland, L.-E., Hervoches, C. H., Erdal, S., Hancke, R., Islam, M. S., Norby, T. & Haugsrud, R. (2012). *J. Mater. Chem.* **22**, 1762–1764.
Malavasi, L., Fisher, C. A. J. & Islam, M. S. (2010). *Chem. Soc. Rev.* **39**, 4370–4387.
Masson, O. & Thomas, P. (2013). *J. Appl. Cryst.* **46**, 461–465.
McCarthy, G. J., Fischer, R. D., Johnson, G. G. & Gooden, C. E. (1972). *Solid State Chemistry*, National Bureau of Standards Special Publication 364, pp. 397–411. Washington, DC: US Government Printing Office.
Norby, T. (2007). *J. Chem. Eng. Jpn*, **40**, 1166–1171.
Pergolesi, D., Fabbri, E., D'Epifanio, A., Di Bartolomeo, E., Tebano, A., Sanna, S., Licoccia, S., Balestrino, G. & Traversa, E. (2010). *Nat. Mater.* **9**, 846–852.
Ravel, B. & Newville, M. (2005). *J. Synchrotron Rad.* **12**, 537–541.
Scherb, T. (2011). PhD thesis, Technische Universität Berlin, Germany.
Seeger, J., Ivanova, M. E., Meulenberg, W. A., Sebold, D., Stöver, D., Scherb, T., Schumacher, G., Escolástico, S., Solís, C. & Serra, J. M. (2013). *Inorg. Chem.* **52**, 10375–10386.
Shimura, T. (2001). *Solid State Ionics*, **143**, 117–123.
Shoemaker, D. P., Seshadri, R., Hector, A. L., Llobet, A., Proffen, T. & Fennie, C. J. (2010). *Phys. Rev. B*, **81**, 144113.
Solís, C., Escolastico, S., Haugsrud, R. & Serra, J. M. (2011). *J. Phys. Chem. C*, **115**, 11124–11131.
Steele, D. & Fender, B. E. F. (1974). *J. Phys. C Solid State Phys.* **7**, 1–11.
Toby, B. H. (2001). *J. Appl. Cryst.* **34**, 210–213.
Yang, L., Wang, S., Blinn, K., Liu, M., Liu, Z., Cheng, Z. & Liu, M. (2009). *Science*, **326**, 126–129.